# Closed-loop AI enables time- and resource-efficient optimization of processing pathways without microstructural input

# Supplementary Information

## SI 1 Supplementary Results and Data

### SI 1.1 Processing-pathway dataset and experimental record

The initial dataset comprised 40 experimentally produced conditions of the same ZX10 alloy, derived from three cumulative parent states: conventionally extruded (EXT), equal-channel angular pressed (ECAP), and solution-treated (ST), as described in the main Methods. Subsequent cold rolling and thermal treatments were applied individually or sequentially to generate distinct processing pathways.

Each condition was recorded using its ordered processing history. Cold rolling is denoted by $\mathrm{CR}(\varepsilon, \dot{\varepsilon})$, where $\varepsilon$ and $\dot{\varepsilon}$ represent the logarithmic thickness strain and nominal strain rate, respectively. The logarithmic thickness strain was calculated as

$$\varepsilon = \ln\left(\frac{h_0}{h_f}\right), \tag{1}$$

where $h_0$ and $h_f$ are the specimen thicknesses immediately before and after the corresponding rolling stage. The nominal rolling strain rate was calculated as

$$\dot{\varepsilon} = \frac{\varepsilon}{T_{\mathrm{pass}}} = \frac{\ln(h_0/h_f)}{T_{\mathrm{pass}}}, \tag{2}$$

where $T_{\mathrm{pass}}$ is the time required for the specimen to pass through the roll gap, approximately 2.00 s for specimens 10 mm in length. These values represent nominal average strain rates rather than instantaneous strain rates within the roll gap.

Thermal treatment is denoted by $\mathrm{HT}(T, t)$, where $T$ and $t$ represent the treatment temperature and duration, respectively. All processing operations are listed chronologically from left to right. The complete processing histories and corresponding hardness and 24-h corrosion measurements for the initial 40 conditions are reported in Table SI 1.

Table SI 1: **Processing histories and measured properties of the 40 initial ZX10 conditions.** The extruded (EXT), equal-channel angular pressed (ECAP), and solution-treated (ST) parent states are described in the main Methods. Subsequent operations are listed chronologically using $\mathrm{CR}(\varepsilon, \dot{\varepsilon})$ for cold rolling at approximately 25 °C and $\mathrm{HT}(T, t)$ for thermal treatment. Temperatures and durations in $\mathrm{HT}(T, t)$ are given in °C and hours, respectively, unless minutes are stated explicitly. Strains and strain rates in $\mathrm{CR}(\varepsilon, \dot{\varepsilon})$ are dimensionless and $\mathrm{s}^{-1}$, respectively. Hardness and 24-h corrosion rates are reported as mean ± standard deviation.

| **Condition** | **Parent state** | **Subsequent processing** | **Hardness (HV)** | **24-h corrosion rate (mm yr$^{-1}$)** |
|---|---|---|---|---|
| *Extruded and thermally treated conditions* | | | | |
| EXT | EXT | None | $62.98 \pm 1.20$ | $4.35 \pm 1.01$ |
| EXT+150A1 | EXT | $\mathrm{HT}(150, 1)$ | $66.67 \pm 2.09$ | $1.98 \pm 0.54$ |
| EXT+150A10 | EXT | $\mathrm{HT}(150, 10)$ | $65.14 \pm 1.34$ | $3.20 \pm 0.46$ |
| EXT+250A1 | EXT | $\mathrm{HT}(250, 1)$ | $60.05 \pm 0.87$ | $1.69 \pm 1.08$ |
| EXT+250A8 | EXT | $\mathrm{HT}(250, 8)$ | $54.97 \pm 1.56$ | $1.64 \pm 0.63$ |
| EXT+370A1 | EXT | $\mathrm{HT}(370, 1)$ | $48.03 \pm 1.65$ | $1.61 \pm 0.48$ |
| *ECAP and thermally treated conditions* | | | | |

*Continued on next page*

Table SI 1 continued

| Condition | Parent state | Subsequent processing | Hardness (HV) | 24-h corrosion rate (mm yr$^{-1}$) |
|---|---|---|---|---|
| ECAP | ECAP | None | $69.76 \pm 0.74$ | $7.78 \pm 0.16$ |
| ECAP+150A1 | ECAP | HT(150, 1) | $71.42 \pm 1.15$ | $6.20 \pm 0.88$ |
| ECAP+150A5 | ECAP | HT(150, 5) | $70.20 \pm 0.88$ | $4.90 \pm 0.39$ |
| ECAP+150A10 | ECAP | HT(150, 10) | $70.42 \pm 1.68$ | $2.49 \pm 1.10$ |
| ECAP+250A1 | ECAP | HT(250, 1) | $68.26 \pm 0.94$ | $3.55 \pm 0.54$ |
| ECAP+250A8 | ECAP | HT(250, 8) | $69.10 \pm 1.39$ | $2.79 \pm 0.62$ |
| ECAP+370A1 | ECAP | HT(370, 1) | $53.29 \pm 1.83$ | $3.38 \pm 1.21$ |
| *Cold-rolled ECAP conditions* | | | | |
| ECAP+R | ECAP | CR(0.08, 0.04) | $69.01 \pm 1.34$ | $8.97 \pm 0.99$ |
| ECAP+R+150A1 | ECAP | CR(0.08, 0.04) → HT(150, 1) | $67.75 \pm 1.44$ | $6.98 \pm 2.39$ |
| ECAP+R+150A10 | ECAP | CR(0.08, 0.04) → HT(150, 10) | $77.15 \pm 2.54$ | $3.64 \pm 1.37$ |
| ECAP+R+250A1 | ECAP | CR(0.08, 0.04) → HT(250, 1) | $68.06 \pm 0.60$ | $4.81 \pm 0.80$ |
| ECAP+R+250A8 | ECAP | CR(0.08, 0.04) → HT(250, 8) | $62.88 \pm 1.78$ | $2.63 \pm 0.36$ |
| ECAP+R+370A1 | ECAP | CR(0.08, 0.04) → HT(370, 1) | $49.65 \pm 1.86$ | $3.33 \pm 1.37$ |
| *Solution-treatment time series* | | | | |
| ST1min | ECAP | HT(450, 1 min) | $66.04 \pm 1.41$ | $4.54 \pm 0.57$ |
| ST2min | ECAP | HT(450, 2 min) | $47.37 \pm 1.34$ | $4.47 \pm 0.22$ |
| ST5min | ECAP | HT(450, 5 min) | $44.94 \pm 2.60$ | $4.39 \pm 0.36$ |
| ST15min | ECAP | HT(450, 15 min) | $48.98 \pm 2.44$ | $4.70 \pm 0.55$ |
| ST30min | ECAP | HT(450, 30 min) | $46.71 \pm 1.52$ | $4.83 \pm 0.60$ |
| ST1 | ECAP | HT(450, 1) | $44.47 \pm 3.33$ | $4.31 \pm 0.44$ |
| ST4 | ECAP | HT(450, 4) | $41.87 \pm 1.74$ | $2.86 \pm 1.00$ |
| ST16 | ECAP | HT(450, 16) | $38.56 \pm 2.77$ | $2.70 \pm 0.16$ |
| ST64 | ECAP | HT(450, 64) | $35.97 \pm 2.31$ | $1.90 \pm 1.00$ |
| ST | ST | None | $35.02 \pm 1.75$ | $1.84 \pm 0.28$ |
| *Thermally treated ST conditions* | | | | |
| ST+150A1 | ST | HT(150, 1) | $46.67 \pm 3.92$ | $2.87 \pm 0.05$ |
| ST+150A10 | ST | HT(150, 10) | $40.41 \pm 2.29$ | $3.81 \pm 1.32$ |
| ST+250A1 | ST | HT(250, 1) | $53.56 \pm 2.00$ | $2.87 \pm 0.20$ |
| ST+250A8 | ST | HT(250, 8) | $44.41 \pm 2.69$ | $2.26 \pm 0.68$ |
| ST+370A1 | ST | HT(370, 1) | $41.20 \pm 2.44$ | $2.82 \pm 0.64$ |
| *Cold-rolled and thermally treated ST conditions* | | | | |
| ST+R | ST | CR(0.29, 0.14) | $68.71 \pm 1.42$ | $4.00 \pm 1.09$ |
| ST+R+150A1 | ST | CR(0.29, 0.14) → HT(150, 1) | $75.81 \pm 3.95$ | $5.34 \pm 0.76$ |
| ST+R+150A10 | ST | CR(0.29, 0.14) → HT(150, 10) | $74.88 \pm 3.32$ | $3.97 \pm 0.87$ |
| ST+R+250A1 | ST | CR(0.29, 0.14) → HT(250, 1) | $68.56 \pm 2.00$ | $11.58 \pm 2.92$ |
| ST+R+250A8 | ST | CR(0.29, 0.14) → HT(250, 8) | $59.71 \pm 2.72$ | $8.65 \pm 3.95$ |
| ST+R+370A1 | ST | CR(0.29, 0.14) → HT(370, 1) | $46.96 \pm 1.54$ | $13.33 \pm 1.98$ |

The closed-loop campaign subsequently added 11 conditions across three experimental rounds, all starting from the ECAP state. Recommended pathways included up to two cold-rolling stages and three thermal treatments, with variations in both processing parameters and operation sequence. Table SI 2 lists the recommended pathways and their experimentally measured properties. Deviations between prescribed and achieved rolling reductions are documented separately in Table SI 3.

Table SI 2: **Model-recommended processing pathways and experimentally measured properties of the 11 closed-loop conditions.** All pathways begin from the ECAP-processed state described in the main Methods. Processing operations are listed chronologically from left to right. Temperatures and durations in $\mathrm{HT}(T, t)$ are given in °C and hours, respectively. Strains and strain rates in $\mathrm{CR}(\varepsilon, \dot{\varepsilon})$ are dimensionless and $\mathrm{s}^{-1}$, respectively. Hardness and 24-h corrosion rates correspond to the experimentally realized conditions and are reported as mean ± standard deviation. Differences between prescribed and achieved rolling reductions are provided in Table SI 3.

| **Condition** | **Post-ECAP processing pathway** | **Hardness (HV)** | **24-h corrosion rate (mm yr$^{-1}$)** |
|---|---|---|---|
| *Round 1* | | | |
| R1-R1 | $\mathrm{HT}(250.00, 5.00) \rightarrow \mathrm{HT}(250.00, 5.00) \rightarrow \mathrm{CR}(0.36, 0.18) \rightarrow \mathrm{HT}(100.00, 24.00)$ | $85.08 \pm 3.40$ | $5.98 \pm 0.37$ |
| R1-R2 | $\mathrm{CR}(0.21, 0.10) \rightarrow \mathrm{HT}(246.44, 6.68) \rightarrow \mathrm{HT}(244.25, 7.91) \rightarrow \mathrm{CR}(0.08, 0.04) \rightarrow \mathrm{HT}(154.54, 21.63)$ | $78.86 \pm 2.60$ | $5.91 \pm 1.03$ |
| R1-R3 | $\mathrm{CR}(0.12, 0.06) \rightarrow \mathrm{HT}(231.45, 6.08) \rightarrow \mathrm{HT}(243.01, 6.69) \rightarrow \mathrm{CR}(0.10, 0.05) \rightarrow \mathrm{HT}(167.46, 17.97)$ | $81.17 \pm 2.37$ | $6.13 \pm 0.55$ |
| R1-R4 | $\mathrm{CR}(4.00 \times 10^{-3}, 2.00 \times 10^{-3}) \rightarrow \mathrm{HT}(238.49, 8.66) \rightarrow \mathrm{HT}(240.46, 5.77) \rightarrow \mathrm{CR}(0.31, 0.15) \rightarrow \mathrm{HT}(183.26, 17.83)$ | $80.59 \pm 3.97$ | $5.90 \pm 0.20$ |
| *Round 2* | | | |
| R2-R1 | $\mathrm{CR}(0.21, 0.10) \rightarrow \mathrm{HT}(186.93, 4.73) \rightarrow \mathrm{HT}(188.98, 4.96) \rightarrow \mathrm{CR}(0.07, 0.04) \rightarrow \mathrm{HT}(58.97, 3.66)$ | $92.65 \pm 2.08$ | $3.44 \pm 0.62$ |
| R2-R2 | $\mathrm{CR}(0.16, 0.08) \rightarrow \mathrm{HT}(196.99, 4.13) \rightarrow \mathrm{HT}(198.87, 4.86) \rightarrow \mathrm{CR}(0.09, 0.05) \rightarrow \mathrm{HT}(99.56, 3.55)$ | $89.87 \pm 3.27$ | $4.66 \pm 0.62$ |
| R2-R3 | $\mathrm{CR}(0.20, 0.10) \rightarrow \mathrm{HT}(195.02, 3.80) \rightarrow \mathrm{HT}(197.80, 4.74) \rightarrow \mathrm{CR}(0.07, 0.03) \rightarrow \mathrm{HT}(85.32, 4.08)$ | $100.50 \pm 5.36$ | $3.40 \pm 0.82$ |
| R2-R4 | $\mathrm{CR}(0.14, 0.07) \rightarrow \mathrm{HT}(194.21, 4.88) \rightarrow \mathrm{HT}(191.34, 4.95) \rightarrow \mathrm{CR}(0.06, 0.03) \rightarrow \mathrm{HT}(55.31, 4.25)$ | $87.20 \pm 3.52$ | $3.73 \pm 0.32$ |
| *Round 3* | | | |
| R3-R1 | $\mathrm{CR}(0.10, 0.05) \rightarrow \mathrm{HT}(196.00, 4.80) \rightarrow \mathrm{HT}(196.00, 4.80) \rightarrow \mathrm{CR}(0.02, 0.01) \rightarrow \mathrm{HT}(50.00, 12.00)$ | $95.50 \pm 2.61$ | $3.08 \pm 0.30$ |
| R3-R2 | $\mathrm{CR}(0.01, 5.00 \times 10^{-3}) \rightarrow \mathrm{HT}(196.00, 4.80) \rightarrow \mathrm{HT}(196.00, 4.80) \rightarrow \mathrm{CR}(0.02, 0.01) \rightarrow \mathrm{HT}(50.00, 10.00)$ | $88.44 \pm 1.95$ | $2.40 \pm 0.19$ |
| R3-R3 | $\mathrm{CR}(0.01, 5.00 \times 10^{-3}) \rightarrow \mathrm{HT}(196.00, 4.80) \rightarrow \mathrm{HT}(196.00, 4.80) \rightarrow \mathrm{CR}(0.02, 0.01) \rightarrow \mathrm{HT}(50.00, 12.00)$ | $86.18 \pm 1.75$ | $2.62 \pm 0.69$ |

## SI 1.2 Experimental feasibility and refinement of the processing space

Experimental feasibility was assessed by comparing the model-recommended and experimentally achieved rolling reductions at each deformation stage (Table SI 3). Percentage thickness reduction, $r$, was calculated from the logarithmic strain as

$$r = 100\,(1 - \exp\,[-\varepsilon])\,, \tag{3}$$

where each reduction is referenced to the specimen thickness immediately before the corresponding rolling stage. All recommended thermal-treatment stages were implemented at their prescribed temperatures and durations. Deviations from the recommended pathways therefore arose from the inability to achieve certain rolling reductions.

In Round 1, the largest deviations occurred during the second rolling stage. For R1-R1 and R1-R4, the prescribed reductions of 30.23% and 26.45% were limited to 10.00% and 13.81%, respectively. These results indicated that rolling reductions permitted by the initial bounds could not always be achieved after the preceding thermomechanical operations. The rolling-strain bounds were consequently reduced before Round 2, together with the permitted thermal-treatment durations.

Table SI 3: **Recommended and experimentally achieved thickness reductions for the cold-rolling operations.** Values are percentages of the specimen thickness immediately before each rolling stage.

| Condition | First rolling stage | | Second rolling stage | |
|---|---|---|---|---|
| | Recommended (%) | Achieved (%) | Recommended (%) | Achieved (%) |
| *Round 1* | | | | |
| R1-R1 | – | – | 30.23 | 10.00 |
| R1-R2 | 18.69 | 13.33 | 7.85 | 8.12 |
| R1-R3 | 10.92 | 10.37 | 9.80 | 5.37 |
| R1-R4 | 0.40 | 0.74 | 26.45 | 13.81 |
| *Round 2* | | | | |
| R2-R1 | 19.16 | 18.78 | 17.37 | 6.95 |
| R2-R2 | 12.77 | 14.44 | 16.29 | 8.82 |
| R2-R3 | 17.28 | 18.21 | 22.04 | 6.48 |
| R2-R4 | 13.18 | 13.33 | 15.66 | 5.54 |
| *Round 3* | | | | |
| R3-R1 | 9.52 | 9.52 | 1.98 | 1.98 |
| R3-R2 | 1.00 | 1.00 | 1.98 | 1.98 |
| R3-R3 | 1.00 | 1.00 | 1.98 | 1.98 |

In Round 2, all first-stage rolling reductions were achieved close to their prescribed values, whereas the recommended second-stage reductions of 15.66–22.04% were limited to 5.54–8.82%. This distinction localized the remaining feasibility constraint to the later deformation stage, allowing its upper strain bound to be reduced independently before Round 3.

Following this refinement, all recommended rolling reductions in Round 3 were achieved as prescribed, with first-stage reductions of 1.00–9.52% and a common second-stage reduction of 1.98%. These results demonstrate that the experimentally accessible deformation range depended on the position of rolling within the processing sequence. Stage-specific feasibility feedback therefore enabled the search space to be progressively refined toward fully executable processing pathways.

## SI 1.3 Closed-loop model results

The processing bounds were refined between rounds based on experimental feasibility and the measured property responses (Table SI 4).

Table SI 4: **Optimization objectives and processing constraints across three closed-loop rounds.** Processing bounds were progressively refined based on experimental feasibility and the property responses obtained in preceding rounds.

| Parameter | Round 1 | Round 2 | Round 3 |
|---|---|---|---|
| Optimization objective | Maximize $H/CR$ | Separate $H$ and $CR$ | Separate $H$ and $CR$ |
| Strain descriptor | 0–0.36 | 0–0.25 | $\varepsilon_1$: 0.01–0.20; $\varepsilon_2$: 0.01–0.02 |
| Heat-treatment temperature (°C) | 100–250 | 50–200 | 50–200 |
| Heat-treatment duration (h) | 5–24 | 3–10 | 1–12 |

$\varepsilon_1$ and $\varepsilon_2$ denote the first and second rolling strains, respectively.

The surrogate models were updated between experimental rounds by incorporating the newly measured processing–property responses. The training dataset increased from 40 initial conditions to 44 and 48 conditions before Rounds 2 and 3, respectively, and comprised 51 experimentally evaluated conditions upon

completion of the optimization. The round-specific optimization objectives and refinements to the processing space are summarized in Table SI 5.

Prior to Round 3, LASSO regression was performed using the available experimental data to examine the associations between individual processing descriptors and the measured hardness and corrosion rate. The resulting coefficient magnitudes are presented in Figure SI 1. The analysis revealed different dependencies for the two properties, with the final heat-treatment temperature exhibiting the largest coefficient magnitude for corrosion rate and the rolling strains exhibiting the largest magnitudes for hardness.

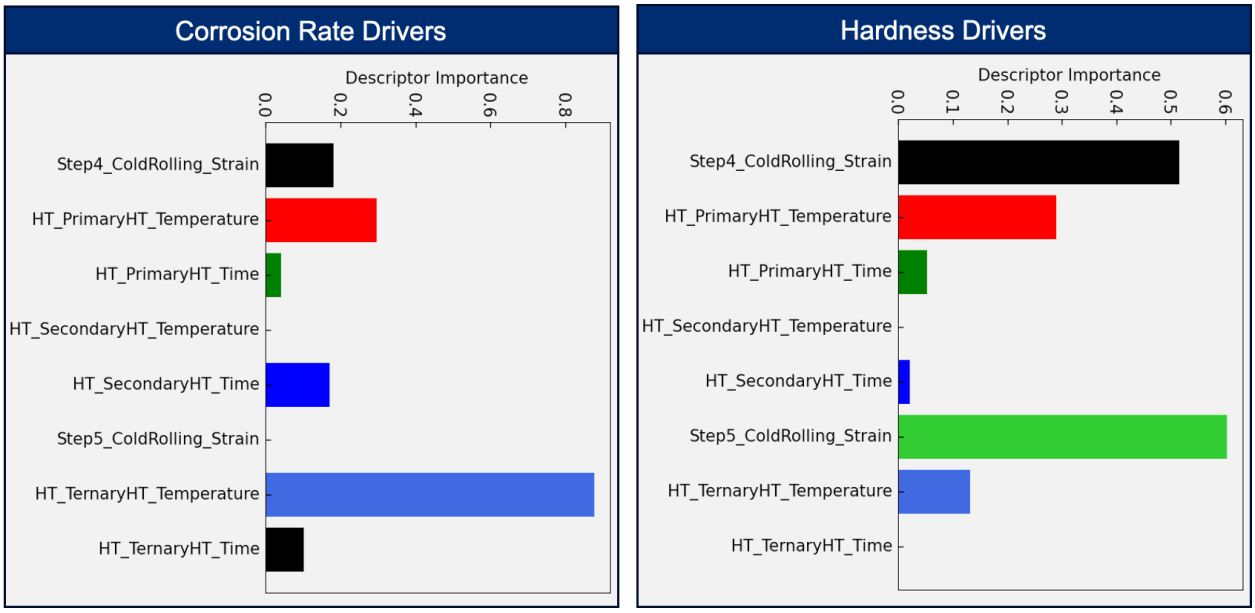



Figure SI 1: **LASSO regression coefficients for stage-specific processing descriptors prior to Round 3.** Magnitudes of the LASSO coefficients obtained for (a) corrosion rate and (b) hardness using the experimental data available after Round 2. The final heat-treatment temperature exhibits the largest coefficient magnitude for corrosion rate, whereas the rolling strains, particularly that of the second rolling stage, exhibit the largest magnitudes for hardness.

Table SI 5: **Round-specific configuration of the closed-loop search.** The training-set size refers to the number of experimentally measured conditions available at the beginning of each round.

| Round | Training conditions | Optimization objective | Processing representation | No. of recommendations |
|---|---|---|---|---|
| 1 | 40 | Maximize the hardness-to-corrosion-rate ratio | Ordered processing histories evaluated within the initial processing bounds | 4 |
| 2 | 44 | Maximize hardness and minimize corrosion as separate objectives | Ordered processing histories evaluated within feasibility-refined bounds | 4 |
| 3 | 48 | Maximize hardness and minimize corrosion as separate objectives | Stage-specific processing descriptors evaluated within further refined bounds | 3 |

### SI 1.3.1 Predicted and experimentally measured responses

Model predictions were compared with the experimentally measured responses for all 11 recommended conditions. The predictions correspond to those generated before experimental evaluation in each round. Round 1 employed the hardness-to-corrosion-rate ratio as its optimization objective, whereas Rounds 2 and 3 considered hardness and corrosion rate separately.

Table SI 6: **Predicted and experimentally measured hardness-to-corrosion-rate ratios in Round 1.** The measured ratios were calculated from the mean experimental hardness and 24-h corrosion rate of each condition.

| Condition | Predicted ratio | Measured ratio |
|---|---|---|
| R1-R1 | 74.00 | 14.22 |
| R1-R2 | 64.30 | 13.35 |
| R1-R3 | 61.51 | 13.25 |
| R1-R4 | 61.37 | 13.67 |

Table SI 7: **Model-predicted and experimentally measured hardness and 24-h corrosion rates in Rounds 2 and 3.** Experimental measurements are reported as mean ± standard deviation. Predictions are the model-generated point estimates before experimental evaluation. Measured properties correspond to the experimentally realized processing conditions.

| Condition | Hardness (HV) | | Corrosion rate (mm $yr^{-1}$) | |
|---|---|---|---|---|
| | Predicted | Measured | Predicted | Measured |
| *Round 2* | | | | |
| R2-R1 | 77.04 | $92.65 \pm 2.08$ | 0.279 | $3.44 \pm 0.62$ |
| R2-R2 | 76.27 | $89.87 \pm 3.27$ | 1.139 | $4.66 \pm 0.62$ |
| R2-R3 | 77.41 | $100.50 \pm 5.36$ | 0.613 | $3.40 \pm 0.82$ |
| R2-R4 | 78.34 | $87.20 \pm 3.52$ | 0.114 | $3.73 \pm 0.32$ |
| *Round 3* | | | | |
| R3-R1 | 81.84 | $95.50 \pm 2.61$ | 1.368 | $3.08 \pm 0.30$ |
| R3-R2 | 72.51 | $88.44 \pm 1.95$ | 2.490 | $2.40 \pm 0.19$ |
| R3-R3 | 72.92 | $86.18 \pm 1.75$ | 1.258 | $2.62 \pm 0.69$ |

The predicted and measured responses exhibited substantial differences, particularly during the early experimental rounds. Round 1 substantially overpredicted the hardness-to-corrosion-rate ratio for all four recommendations. In Round 2, hardness was consistently underpredicted, while predicted corrosion rates were substantially lower than the experimental measurements. Round 3 showed improved agreement for corrosion, particularly for R3-R2, although hardness remained systematically underpredicted.

These comparisons should also be considered in the context of experimental feasibility. Several recommended rolling reductions in Rounds 1 and 2 could not be fully realized, such that the measured responses corresponded to pathways that differed from those originally prescribed. The prediction discrepancies therefore reflect both model limitations and differences between recommended and experimentally achieved processing histories.

## SI 1.4 Microstructural characterization of the selected states

Post-search microstructural characterization was performed on R3-R2 and R3-R3 to compare grain size and morphology, grain-boundary misorientation, local lattice curvature, second-phase distribution and composition, and crystalline phase constitution.

### SI 1.4.1 Grain size and morphology

Both conditions exhibited fine to ultrafine-grained structures with right-skewed grain-size distributions (Figure SI 2). Most fitted-ellipse major-axis diameters were below approximately 2 $\mu$m, with distribution tails extending to 4.0–4.5 $\mu$m.

The mean fitted-ellipse major-axis diameters were $1.68 \pm 0.69$ $\mu$m for R3-R2 and $1.36 \pm 0.71$ $\mu$m for R3-R3, respectively. Although the distribution for R3-R3 was shifted toward smaller grain sizes, the two distributions overlapped substantially.

Both aspect-ratio distributions were concentrated near 1.2–1.5, with tails extending beyond 3. Mean fitted-ellipse aspect ratios were 1.64 for R3-R2 and 1.79 for R3-R3, indicating predominantly equiaxed to mildly elongated grain sections, together with smaller populations of more elongated grains. These measurements characterize two-dimensional grain sections and do not establish the corresponding three-dimensional grain morphologies.

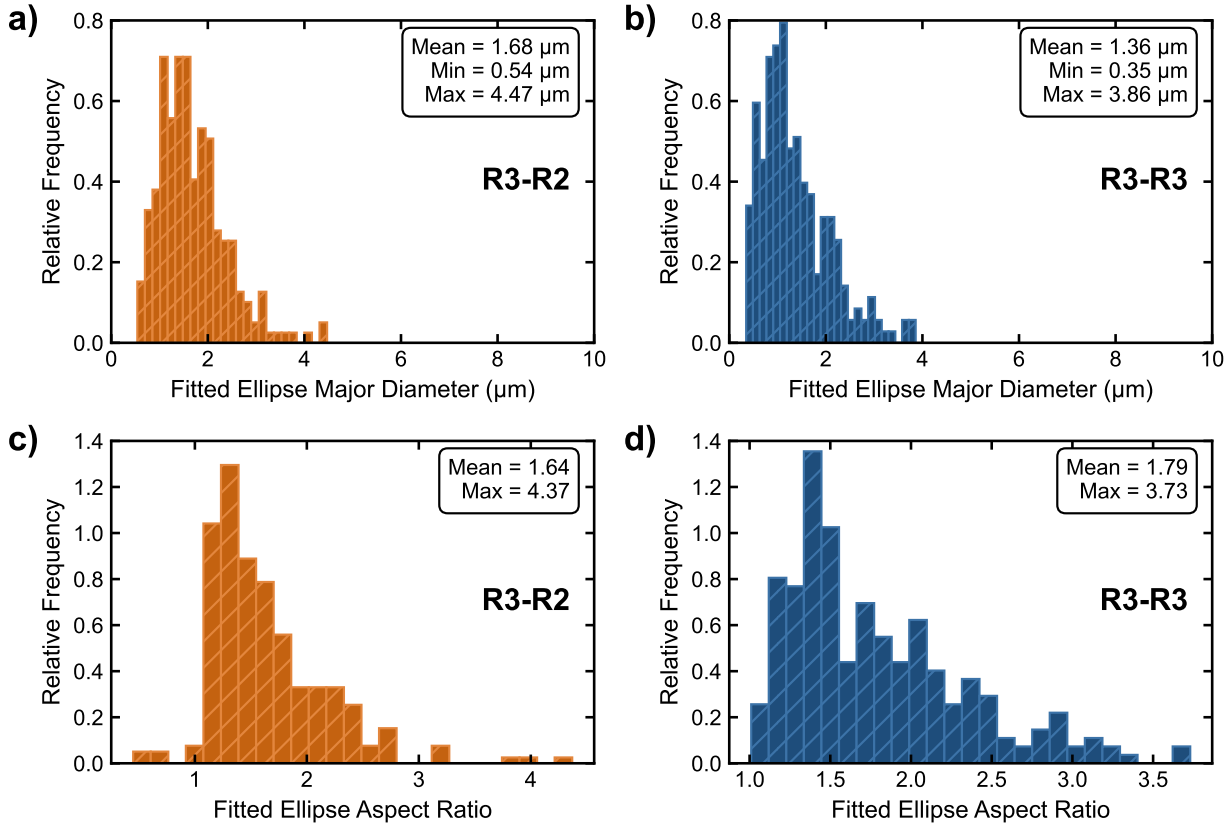



Figure SI 2: **Grain-size and grain-shape distributions of R3-R2 and R3-R3.** Distributions of fitted-ellipse major diameter (**a**, **b**) and fitted-ellipse aspect ratio (**c**, **d**) for R3-R2 (**a**, **c**) and R3-R3 (**b**, **d**). Inset boxes report the mean, minimum, and maximum values for each distribution. Grain boundaries were defined using a minimum misorientation angle of 10°, and grains intersecting the map boundaries were included in the analysis.

### SI 1.4.2 Grain-boundary misorientation

Grain-boundary misorientation distributions were broadly comparable between R3-R2 and R3-R3 (Figure SI 3), with populations spanning both lower and higher misorientation angles.

Experimental neighbor-pair distributions were compared with distributions generated by randomly pairing orientations within each EBSD dataset and with a theoretical reference for randomly oriented Mg crystals. Random pairing preserves the measured orientation population while removing spatial correlations between

neighboring grains, allowing the influence of local orientation correlations to be distinguished from that of the overall texture.

Both conditions exhibited similar deviations from their random-reference distributions, including an enhanced population of lower-misorientation neighbor pairs. The M-index values were 0.162 for R3-R2 and 0.168 for R3-R3, indicating comparable departures from the theoretical random-misorientation distribution. These observations are consistent with similar grain-boundary misorientation characteristics within the sampled regions, although the distributions alone cannot establish the mechanisms responsible for boundary formation or subsequent recovery.

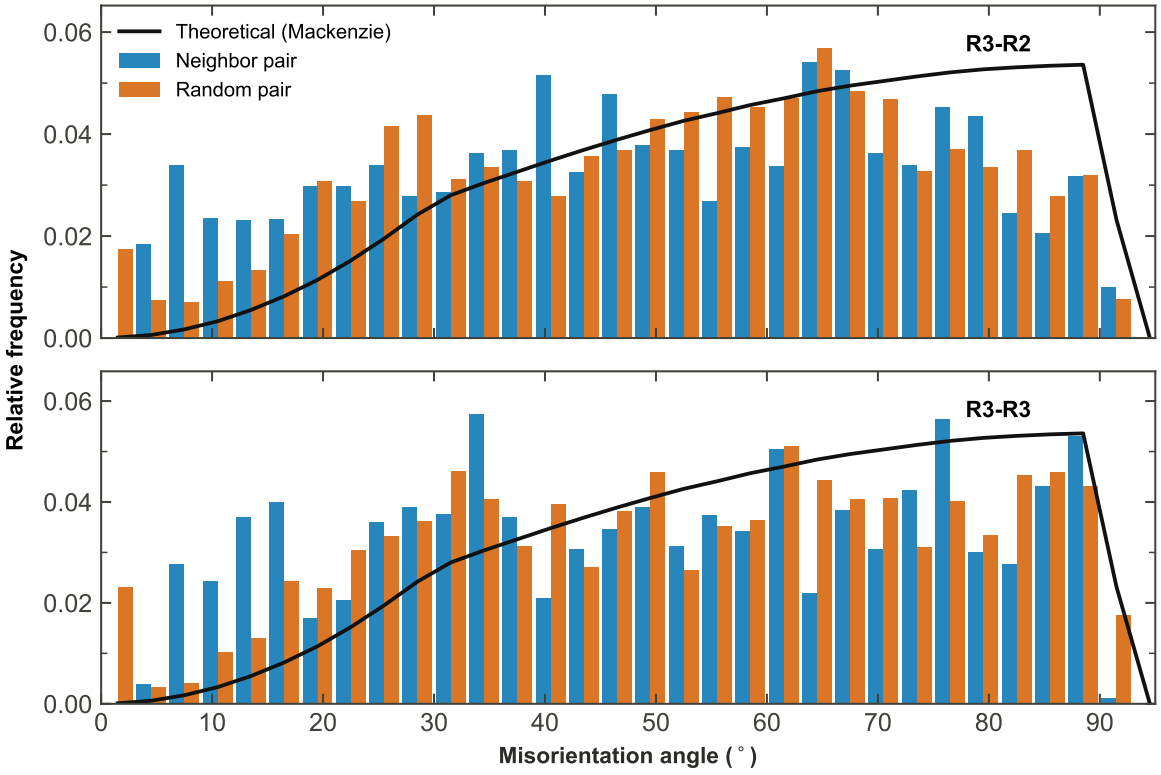



Figure SI 3: **Grain-boundary misorientation distributions of R3-R2 and R3-R3.** Experimental neighbor-pair distributions are compared with distributions generated by randomly pairing orientations from the corresponding EBSD datasets and with a theoretical random-orientation distribution (solid black line), based on the Mackenzie formulation and its generalization to hexagonal crystal symmetry [1, 2]. The random-pair distributions preserve the measured orientation populations while removing spatial correlations between neighboring grains.

### SI 1.4.3 Geometrically necessary dislocation density

Estimated geometrically necessary dislocation (GND) densities were spatially heterogeneous in both conditions (Figure SI 4). The mean estimated densities were $1.012 \times 10^{15}$ m$^{-2}$ for R3-R2 and $6.32 \times 10^{14}$ m$^{-2}$ for R3-R3. Although R3-R2 exhibited a higher mean, the pointwise distributions overlapped broadly and occupied the same order of magnitude. These measurements therefore indicate broadly overlapping GND-density ranges within the analyzed regions rather than establishing distinct or statistically equivalent defect populations.

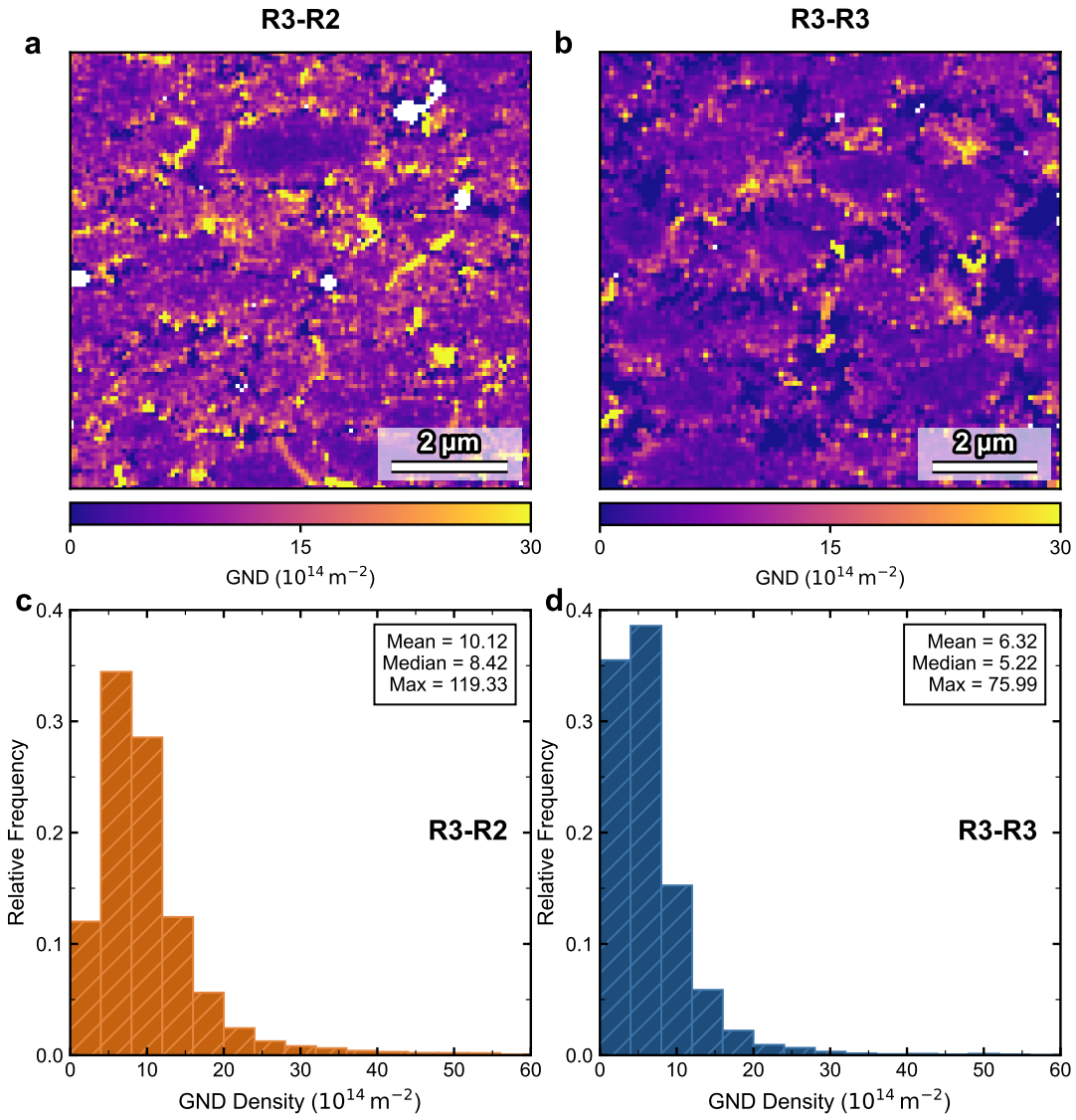



Figure SI 4: **Geometrically necessary dislocation density in R3-R2 and R3-R3.** EBSD-derived GND-density maps (a,b) and corresponding relative-frequency distributions (c,d) for R3-R2 (left) and R3-R3 (right). Both conditions exhibit spatially heterogeneous GND-density distributions of the same order of magnitude, although R3-R3 shows a lower mean GND density and a narrower distribution compared with R3-R2.

### SI 1.4.4 Second-phase distribution and phase characterization

Backscattered-electron images revealed fine, dispersed second-phase particles and occasional coarser particles distributed throughout the Mg matrix in both R3-R2 and R3-R3 (Figure SI 5). The particle populations appeared broadly comparable between the two conditions, without pronounced differences in their spatial distributions. EDS maps showed overlapping Ca and Zn enrichment in the larger particles, consistent with the $Ca_2Mg_6Zn_3$ phase previously identified in ZX10 alloys [3, 4].

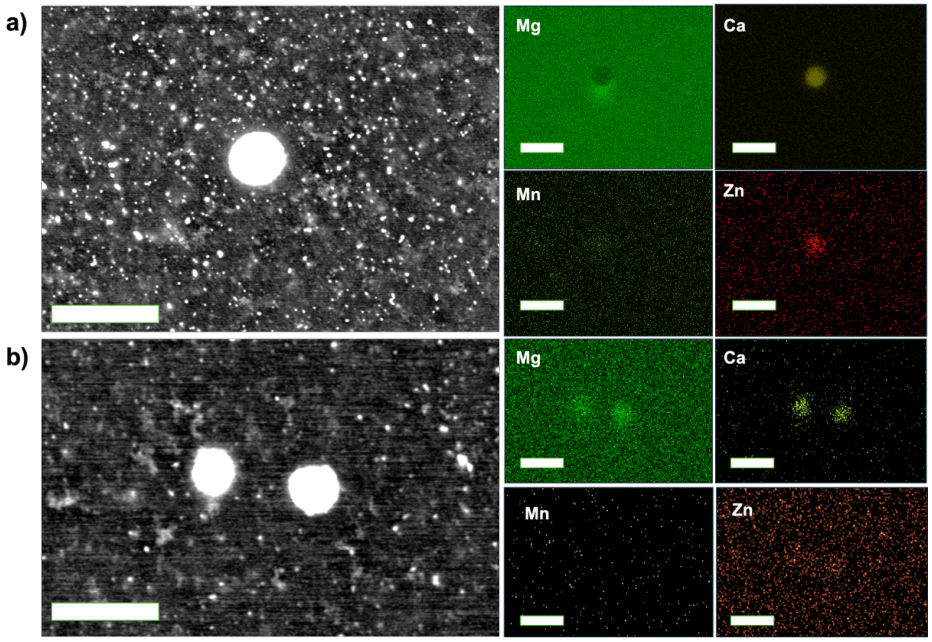



Figure SI 5: **Second-phase distribution and elemental mapping of R3-R2 and R3-R3.** Backscattered-electron micrographs and corresponding EDS maps showing the distributions of Mg, Ca, Mn, and Zn in R3-R2 (upper row) and R3-R3 (lower row). Both conditions contain dispersed fine second-phase features and occasional coarser Ca–Zn-rich particles. Scale bars represent 10 $\mu$m throughout.

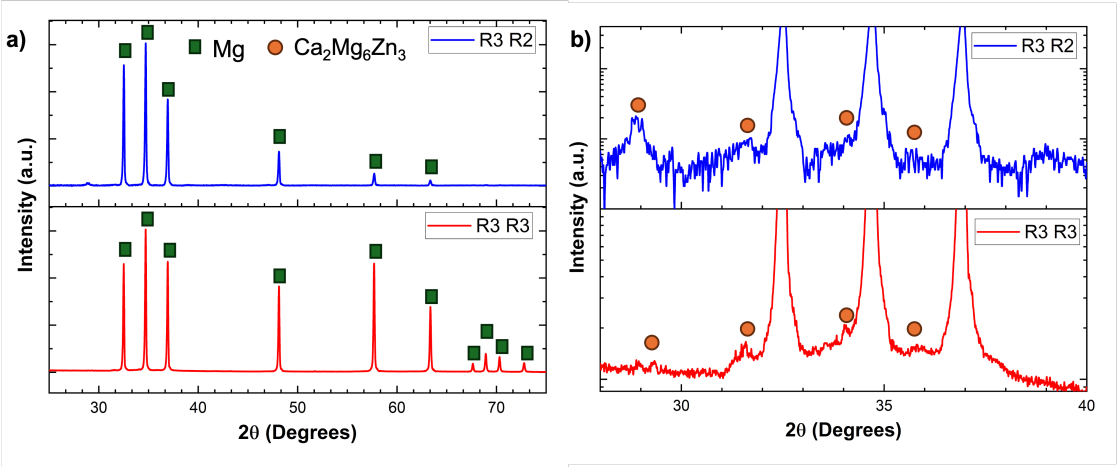



Figure SI 6: **X-ray diffraction patterns of R3-R2 and R3-R3. a,** Full XRD patterns of the two Round 3 conditions, dominated by reflections from the $\alpha$-Mg matrix. Reference reflection positions are shown for Mg and $Ca_2Mg_6Zn_3$. **b,** Enlarged view of the region in logarithm scale between $2\theta = 28°$ and 40°, highlighting the $Ca_2Mg_6Zn_3$ reflections in both conditions.

X-ray diffraction further confirmed the presence of $Ca_2Mg_6Zn_3$ in both conditions (Figure SI 6). The diffraction patterns were dominated by $\alpha$-Mg reflections, with weaker $Ca_2Mg_6Zn_3$ reflections visible in the enlarged $2\theta = 28°$–40° region. The close agreement between the diffraction patterns indicates that R3-R2 and R3-R3 retained similar crystalline phase constitutions, consistent with their comparable second-phase distributions observed by BSE and EDS.

## SI 1.5 Extended mechanical analysis

The ultimate tensile strength, strain to failure and tensile toughness of the selected states are presented in the main text. The supplementary analysis below examines uniform deformation, strain-hardening behavior and fracture morphology, with the solution-treated state (ST) serving as a reference.

### SI 1.5.1 Uniform deformation and strain hardening

The strain-hardening response was evaluated over the uniform plastic-deformation regime before the onset of necking. Engineering stress and strain were converted to true stress and true strain according to

$$\sigma_{\text{true}} = \sigma_{\text{eng}} \left(1 + \varepsilon_{\text{eng}}\right) \tag{4}$$

and

$$\varepsilon_{\text{true}} = \ln\left(1 + \varepsilon_{\text{eng}}\right). \tag{5}$$

The true plastic strain was estimated as

$$\varepsilon_{\text{p,true}} = \varepsilon_{\text{true}} - \frac{\sigma_{\text{true}}}{E_{\text{ref}}}, \tag{6}$$

where $E_{\text{ref}} = 45$ GPa was used as the reference elastic modulus. The uniform plastic-deformation region was fitted using the Hollomon relationship,

$$\sigma_{\text{true}} = K\varepsilon_{\text{p,true}}^{n}, \tag{7}$$

where $K$ is the strength coefficient and $n$ is the strain-hardening exponent. The exponent was obtained from the slope of the linearized relationship

$$\ln\left(\sigma_{\text{true}}\right) = \ln(K) + n\ln\left(\varepsilon_{\text{p,true}}\right). \tag{8}$$

The resulting uniform elongation and strain-hardening exponents are summarized in Table SI 8.

Table SI 8: **Uniform elongation and strain-hardening exponents of the selected conditions.** Values represent mean ± standard deviation from three specimens each for R3-R2 and R3-R3, and two specimens for ST. The apparent strain-hardening exponent was determined from the uniform plastic-deformation regime before necking.

| **Condition** | **Uniform elongation (%)** | **Strain-hardening exponent,** $n$ |
|---|---|---|
| ST | $11.85 \pm 0.62$ | $0.295 \pm 0.054$ |
| R3-R2 | $13.69 \pm 5.46$ | $0.087 \pm 0.015$ |
| R3-R3 | $19.98 \pm 11.30$ | $0.110 \pm 0.038$ |

ST exhibited the highest apparent strain-hardening exponent ($0.295 \pm 0.054$), consistent with its comparatively relaxed and coarse-grained microstructure after prolonged solution treatment. In contrast, R3-R2 and R3-R3 exhibited higher flow stresses but lower exponents, consistent with their ultrafine-grained structures and retained deformation. Despite this reduced apparent strain-hardening capacity, both selected states sustained appreciable uniform elongation, with R3-R3 exhibiting the highest mean value, although with substantial specimen-to-specimen variability. These results highlight that the strain-hardening exponent describes the evolution of flow stress during uniform plastic deformation and does not independently determine the absolute strength or uniform elongation of the material.

### SI 1.5.2 Fracture morphology

The fracture surfaces exhibited distinct morphologies among the three conditions (Figure SI 7). ST showed a mixed fracture morphology with regions containing relatively large dimples, whereas R3-R2 and R3-R3 exhibited predominantly fine, closely spaced dimples characteristic of ductile failure through microvoid nucleation, growth and coalescence.

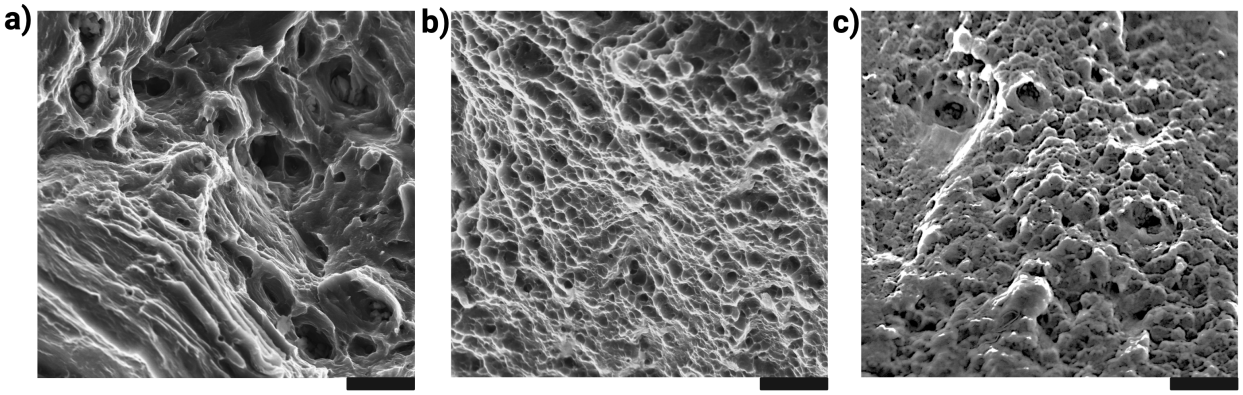



Figure SI 7: **Representative tensile-fracture surfaces of the selected material conditions.** SEM micrographs of **a,** ST, **b,** R3-R2 and **c,** R3-R3 following tensile testing. Scale bars represent 20 $\mu$m.

The observed differences in dimple size corresponded broadly with the grain structures of the three conditions. Previous characterization of ST revealed substantial grain growth following prolonged solution treatment [4], whereas R3-R2 and R3-R3 retained ultrafine-grained structures. The finer dimples observed in the selected states are consistent with their refined grain structures, while their similar fracture morphologies further support their comparable tensile deformation behavior.

## SI 1.6 Post-corrosion surface morphology

To investigate the corrosion mechanisms and resulting surface morphologies, R3-R2 and R3-R3 were examined by scanning electron microscopy following 14 days of immersion in DMEM, EBSS, and HBSS (Figure SI 8). Corrosion products were removed before imaging to reveal the underlying substrate and the spatial distribution of localized attack. Secondary-electron (SE) and backscattered-electron (BSE) images were used to examine the morphology and extent of substrate dissolution.

The DMEM-exposed specimens retained extensive regions of comparatively intact substrate (Figure SI 8a–d). Polishing marks remained visible across substantial portions of both surfaces, while material loss was concentrated in isolated cavities and irregular elongated regions. The relatively limited extent of localized attack was consistent with the lower corrosion rates measured in DMEM.

Following immersion in EBSS, both conditions exhibited more extensive localized corrosion, characterized by circular cavities, annular features, and irregular regions of dissolution (Figure SI 8e–h). R3-R2 contained fewer, relatively well-defined attack sites within the displayed field, whereas R3-R3 exhibited a greater number of smaller cavities and overlapping annular features. These morphologies resemble the pitting and filiform-like corrosion previously observed in ZX10 exposed to chloride-containing EBSS [3].

The HBSS-exposed surfaces also exhibited strongly localized and spatially heterogeneous attack (Figure SI 8i–l). R3-R2 contained a large roughened region with overlapping and coalesced areas of dissolution, whereas R3-R3 retained visible polishing marks over larger portions of the examined surface, with attack concentrated in more isolated regions. These observations demonstrate that localized corrosion can produce different spatial distributions of material loss, even when the overall corrosion rates determined from weight-loss measurements are comparable.

The localized dissolution observed across these environments is consistent with the microgalvanic corrosion mechanisms previously established for ZX10, in which $Ca_2Mg_6Zn_3$ particles act as cathodic sites relative to the surrounding $\alpha$-Mg matrix [3, 4]. The differences in the extent and morphology of attack among DMEM, EBSS, and HBSS further highlight the influence of immersion-medium chemistry on corrosion behavior [5]. Despite local variations in the distribution of corrosion damage, R3-R2 and R3-R3 exhibited broadly similar corrosion morphologies within each medium, consistent with their comparable 14-day corrosion rates.

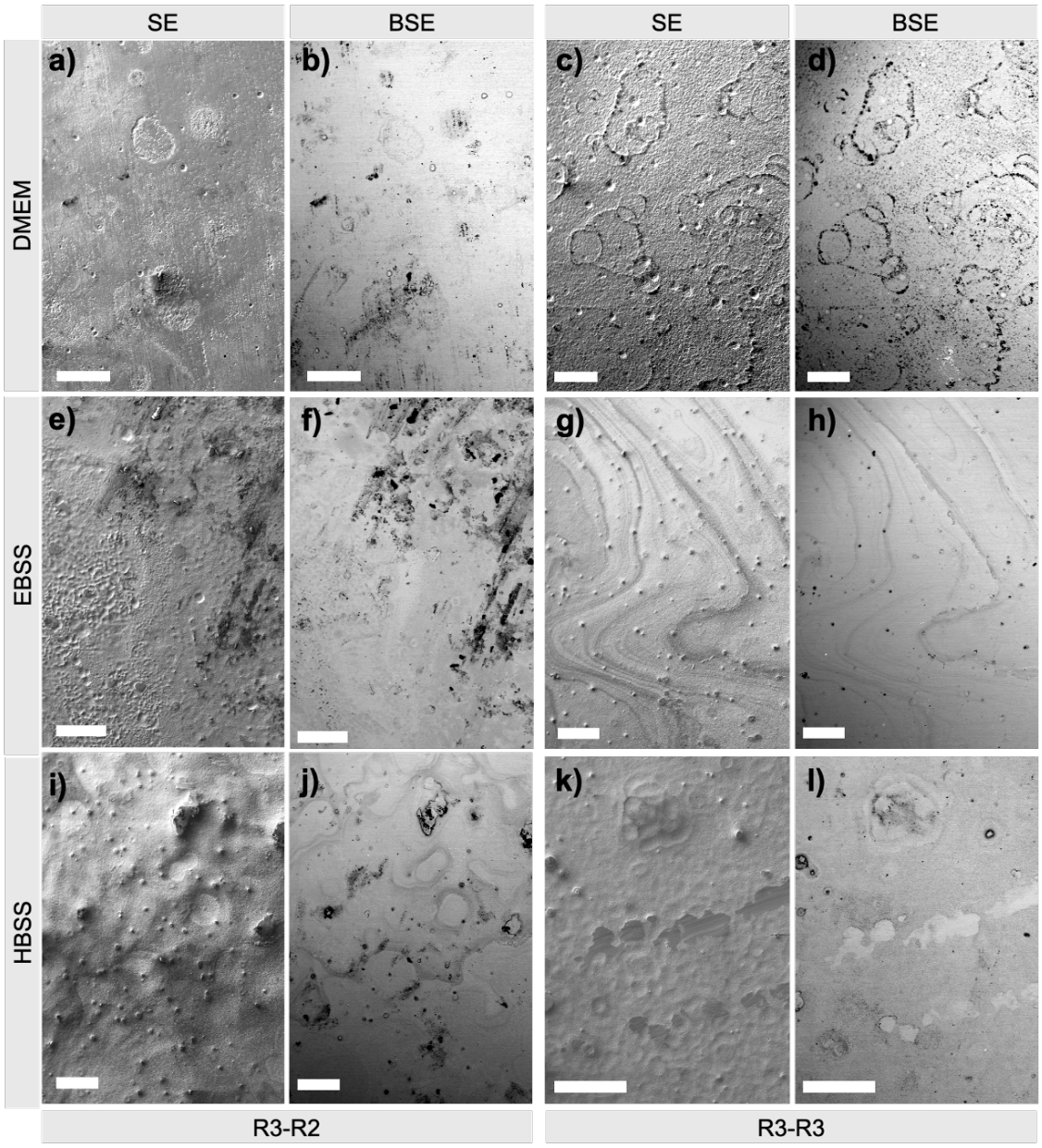



Figure SI 8: **Post-corrosion surface morphologies of the closed-loop-selected conditions.** Paired secondary-electron and backscattered-electron micrographs of R3-R2 and R3-R3 after 14 days of immersion in DMEM (**a**–**d**), EBSS (**e**–**h**) and HBSS (**i**–**l**). Within each medium, the first two panels show R3-R2 and the subsequent two panels show R3-R3, with the secondary-electron image followed by the corresponding backscattered-electron image. All specimens were imaged after removal of the corrosion products. Scale bars represent 200 $\mu$m.

## SI 1.7 Experimental workload analysis

The experimental workload associated with the targeted-characterization strategy was compared with a benchmark in which the same detailed characterization procedures were applied to all 51 experimentally evaluated conditions. This retrospective analysis was used to estimate the researcher time avoided by reserving detailed characterization for the two selected states. The comparison does not imply that conventional

materials studies necessarily characterize every processing condition.

The analysis considered hands-on researcher time associated with specimen preparation, experimental setup, instrument operation, cleaning, data extraction and routine analysis. Unattended processing, immersion periods and automated instrument acquisition were excluded, as these activities did not require continuous researcher involvement. Material processing and sample production were also excluded because they were common to both approaches.

Workload estimates were reconstructed from the experimental procedures used in this study and expressed as approximate ranges to account for variations in specimen preparation, instrument setup and analysis requirements (Table SI 9). Rapid hardness and 24-h corrosion measurements required an estimated 2–3 h of active researcher time per condition, whereas the additional metallographic preparation, EBSD, SEM-BSE/EDS and XRD characterization required approximately 4–6 h per condition.

Table SI 9: **Estimated hands-on researcher time for the experimental measurements.** Estimates were reconstructed from the experimental procedures used in this study and are reported as approximate ranges. Unattended immersion, processing and automated acquisition are excluded.

| **Activity** | **Included work** | **Hands-on time per condition** |
|---|---|---|
| Hardness | Surface preparation, instrument operation, indentation verification and data extraction | Approximately 1 h |
| 24-h corrosion | Specimen preparation, weighing, immersion setup, cleaning and data entry | Approximately 1–2 h |
| Metallographic preparation | Mounting, grinding and polishing for EBSD and electron microscopy | Approximately 1–2 h |
| EBSD | Instrument setup, alignment, pattern optimization, acquisition oversight and routine analysis | Approximately 2–3 h |
| SEM-BSE/EDS and XRD | Specimen loading, imaging or scan setup, compositional mapping and routine data inspection | Approximately 1 h |
| Property-feedback total | Hardness and 24-h corrosion | Approximately 2–3 h |
| Detailed-characterization total | Metallographic preparation, EBSD, SEM-BSE/EDS and XRD | Approximately 4–6 h |

Applying the rapid property-feedback measurements to all 51 conditions required an estimated

$$T_{\text{feedback}} = 51(2\text{–}3) \approx 100\text{–}150 \text{ researcher h.} \tag{9}$$

Applying the detailed-characterization procedures to all 51 conditions would have required approximately

$$T_{\text{characterize-all}} = 51(4\text{–}6) \approx 200\text{–}300 \text{ researcher h.} \tag{10}$$

In contrast, detailed characterization of only R3-R2 and R3-R3 required an estimated 8–12 researcher-hours. The corresponding workload avoided by characterizing two rather than 51 conditions was therefore

$$T_{\text{avoided}} = (51 - 2)(4\text{–}6) \approx 200\text{–}300 \text{ researcher h.} \tag{11}$$

This targeted approach reduced the number of detailed-characterization packages by approximately 96%, avoiding 49 condition-level characterization packages. Considering EBSD, SEM-BSE/EDS and XRD separately, this corresponds to approximately 150 fewer condition-technique applications, with associated reductions in specimen preparation, instrument use and data analysis.

Micro-tensile testing and 14-day corrosion testing were excluded from the comparison because they were performed as final validation rather than as feedback during optimization. Unsuccessful measurements, unattended instrument occupancy, and scheduling delays were also excluded. The estimated 200–300 researcher-hours avoided therefore represent a retrospective comparison of active experimental effort rather than a direct measurement of calendar-time acceleration.

# SI 2 Supplementary Methods

## SI 2.1 Microstructural data processing and analysis

The experimental techniques and instrumentation used for post-search microstructural characterization are described in the main Methods. Additional data-processing and analysis procedures are provided below.

For electron backscatter diffraction (EBSD), polished specimens were ion-beam milled before measurement to minimize residual surface deformation and improve diffraction-pattern quality. The orientation datasets were processed using AZtecCrystal software. Grains were reconstructed using a minimum boundary misorientation angle of 10°, with grains intersecting the map boundaries retained in the analysis. Grain morphology was evaluated by fitting an ellipse to each reconstructed grain and extracting its major-axis diameter and aspect ratio. Arithmetic means, standard deviations, and area-weighted mean diameters were calculated from the grain-level measurements.

Grain-boundary misorientation distributions were calculated from neighboring grain pairs. These distributions were compared with those obtained by randomly pairing orientations from the corresponding EBSD datasets, thereby preserving the measured orientation populations while removing their spatial relationships. A theoretical distribution for randomly oriented Mg crystals was included as a reference. The M-index was calculated from the deviation between the experimental and theoretical misorientation distributions. Identical grain-reconstruction and analysis procedures were applied to R3-R2 and R3-R3.

Geometrically necessary dislocation (GND) density was estimated from local lattice curvature using the weighted Burgers-vector method [6] implemented in AZtecCrystal. Calculations were performed using circular $3\times3$ kernels and an EBSD step size of 0.3 $\mu$m. Mean densities were obtained from valid measurement points within each analyzed region, and the pointwise distributions were retained for comparison. Identical filtering and calculation parameters were applied to both conditions. These estimates represent lattice curvature resolved by EBSD and do not include statistically stored dislocations.

Backscattered-electron images and energy-dispersive X-ray spectroscopy (EDS) maps were analyzed following procedures established previously for ZX10 magnesium alloys [3, 4]. Images used for comparison were acquired under comparable magnification and contrast conditions. Backscattered-electron images were used to examine second-phase morphology and spatial distribution, while EDS maps were used to evaluate the distributions of Mg, Ca, Mn, and Zn.

X-ray diffraction (XRD) measurements were performed using a Malvern Panalytical Aeris diffractometer operated at 40 kV and 7.5 mA. Patterns were collected over a $2\theta$ range of approximately 20°–90° using a step size of 0.002° and two scan summations. Quantitative phase-fraction determination and line-profile analysis were not performed.

## SI 2.2 Additional tensile and corrosion procedures

### SI 2.2.1 Tensile data processing and mechanical-property extraction

Micro-tensile specimen preparation, testing conditions, and digital image correlation (DIC) measurements are described in the main Methods, following previously established procedures [3]. Additional details of the stress–strain data processing are provided here.

A randomly distributed black speckle pattern was applied over a uniform white background on the polished gauge surfaces. Recorded videos were converted into sequential image frames, typically extracting every 10th–20th frame depending on test duration and the required temporal resolution. Load data were baseline-corrected using the initial unloaded region, and engineering stress was calculated as

$$\sigma_{\mathrm{eng}} = \frac{P_{\mathrm{corr}}}{A_0}, \tag{12}$$

where $P_{\mathrm{corr}}$ is the baseline-corrected load and $A_0$ is the initial specimen cross-sectional area.

The load and image records were synchronized by mapping the first and final analyzed images onto the corresponding tensile-test interval and linearly interpolating the load-derived stress to the image time points. Two-dimensional DIC was performed using VIC-2D software (Correlated Solutions), with the average axial engineering strain obtained from the deforming gauge region.

The resulting stress–strain curves were inspected for low-strain tracking instabilities, frame-to-frame noise, and post-fracture artifacts. Mild Savitzky–Golay smoothing, typically using a five-point window, was applied for quantitative property extraction [7, 8]. Fracture was identified from the unsmoothed load or stress response, and post-fracture DIC points were excluded from the analysis.

Ultimate tensile strength was defined as the maximum engineering stress, uniform elongation as the engineering strain at maximum stress, and strain to failure as the final valid strain before fracture. Tensile toughness was determined from the area under the engineering stress–strain curve:

$$U = \int_0^{\varepsilon_f} \sigma_{\mathrm{eng}}\, d\varepsilon_{\mathrm{eng}}, \tag{13}$$

where $\varepsilon_f$ is the engineering strain to failure. The apparent strain-hardening exponent was determined using the true-stress and true-plastic-strain transformations and Hollomon relationship described in Section SI 1.5.1.

### SI 2.2.2 Additional corrosion-testing procedures

The 24-h and 14-day immersion conditions, specimen replication, and weight-loss-based corrosion-rate calculations are described in the main Methods, following established procedures [3–5]. Corrosion products were removed according to ASTM G1 [9]. Specimens were subsequently rinsed, dried, and reweighed before calculating corrosion rates from weight loss.

For the 14-day immersion experiments, solution pH was measured daily. The immersion medium was replaced when the pH approached 8.0 rather than according to a fixed schedule. Under the conditions used here, replacement was typically required approximately every second day. Representative post-corrosion surfaces were examined by secondary-electron and backscattered-electron imaging after removal of the corrosion products.

---

# References


[1] J Mackenzie, "Second paper on statistics associated with the random disorientation of cubes", Biometrika **45**, 229–240 (1958).

[2] J Mason and CA Schuh, "The generalized mackenzie distribution: disorientation angle distributions for arbitrary textures", Acta Materialia **57**, 4186–4197 (2009).

[3] S Raguraman, A Kim, T Ayodeji, AJ Griebel, D Bershadsky, T Nguyen, and TP Weihs, "Simultaneous Optimization of Strength and Bio-Corrosion Resistance in Biodegradable ZX10 Magnesium Alloy via Thermomechanical Processing and Annealing", Journal of Alloys and Compounds, 180078 (2025).

[4] S Raguraman, MS Priyadarshini, T Nguyen, R McGovern, A Kim, AJ Griebel, P Clancy, and TP Weihs, "Machine learning-guided accelerated discovery of structure-property correlations in lean magnesium alloys for biomedical applications", Journal of Magnesium and Alloys, 10.1016/j.jma.2024.06.008 (2024).

[5] S Raguraman, B Ulugun, T Ayodeji, R Chowdhury, A Griebel, and T Weihs, "Evaluating In-Vitro Corrosion Testing of ECAP-Processed Lean Magnesium Alloys: The Critical Role of Degradation Media Composition, Buffering, and Volume", JOM, 10.1007/s11837-025-07176-7 (2025).

[6] J Wheeler, E Mariani, S Piazolo, D Prior, P Trimby, and M Drury, "The weighted Burgers vector: a new quantity for constraining dislocation densities and types using electron backscatter diffraction on 2D sections through crystalline materials", Journal of Microscopy **233**, 482–494 (2009).

[7] A Savitzky and MJ Golay, "Smoothing and differentiation of data by simplified least squares procedures.", Analytical chemistry **36**, 1627–1639 (1964).

[8] P Virtanen, R Gommers, TE Oliphant, M Haberland, T Reddy, D Cournapeau, E Burovski, P Peterson, W Weckesser, J Bright, SJ van der Walt, M Brett, J Wilson, KJ Millman, N Mayorov, ARJ Nelson, E Jones, R Kern, E Larson, CJ Carey, İ Polat, Y Feng, EW Moore, J VanderPlas, D Laxalde, J Perktold, R Cimrman, I Henriksen, EA Quintero, CR Harris, AM Archibald, AH Ribeiro, F Pedregosa, P van Mulbregt, and SciPy 1.0 Contributors, "SciPy 1.0: Fundamental Algorithms for Scientific Computing in Python", Nature Methods **17**, 261–272 (2020).

[9] G01 Committee, *Practice for Preparing, Cleaning, and Evaluating Corrosion Test Specimens.*